the complexation of Th. The present result ascertains that a similar tendency is observed also in the group-5 elements. According to theoretical calculations [38], the order of the complex formation of $[MF_6]^-$ (M = Nb, Ta, Db, and Pa) is predicted to be Pa $\gg$ Nb > Db > Ta that is defined by a predominant electrostatic energy of the metal–ligand interaction. In the present case, however, chemical forms of the group-5 elements are not determined as mentioned, although some species are reported to be presumably $[MF_6]^-$, $[MF_7]^{2-}$, and/or $[MF_8]^{3-}$ in 13.9 M HF. Thus, we have to determine the chemical forms of these elements to compare the experimental adsorption sequence with that from predictions.

4. Conclusions

The distribution coefficients of Db and its lighter homologues of the group-5 elements Nb and Ta, and the pseudo-homologue Pa were measured by anion-exchange chromatography. It was found that the adsorption of Db on the anion-exchange resin was evidently smaller than those of Nb and Ta, while it was larger than that of Pa: Ta $\approx$ Nb > Db $\geq$ Pa at 13.9 M HF.

Acknowledgment. The authors express their gratitude to the crew of the JAEA tandem accelerator for their invaluable assistance in the course of these experiments. This work was supported in part by the JAEA-University Collaboration Research Project and the Program on the Scientific Cooperation between JAEA and GSI in Research and Development in the Field of Ion Beam Application.

References

1. Schädel, M. (ed.): *The Chemistry of Superheavy Elements*. Kluwer Academic Publishers, Dordrecht (2003).
2. Kratz, J. V.: Critical evaluation of the chemical properties of the transactinide elements. Pure Appl. Chem. **75**, 103 (2003).
3. Kratz, J. V.: Chemistry of Transactinides. In: *Handbook of Nuclear Chemistry*. Vol. 2 (Vértes, A., Nagy, S., Klencsár, Z., eds.) Kluwer Academic Publishers, Dordrecht (2003), p. 323.
4. Schädel, M.: Chemistry of superheavy elements. Angew. Chem. Int. Ed. **45**, 368 (2006).
5. Hoffman, D. C., Lee, D. M., Pershina, V.: Transactinide elements and future elements. In: *The Chemistry of the Actinides and Transactinide Elements*. 3rd Edn., Vol. 3 (Morss, L. R., Edelstein, N. M., Fuger, J., eds.) Springer, Dordrecht (2006), p. 1652.
6. Eichler, R., Aksenov, N. V., Belozerov, A. V., Bozhikov, G. A., Chepigin, V. I., Dmitriev, S. N., Dressler, R., Gäggeler, H. W., Gorshkov, V. A., Haenssler, F., Itkis, M. G., Laube, A., Lebedev, V. Ya., Malyshev, O. N., Oganessian, Yu. Ts., Petrushkin, O. V., Piguet, D., Rasmussen, P., Shishkin, S. V., Shutov, A. V., Svirikhin, A. I., Tereshatov, E. E., Vostokin, G. K., Wegrzecki, M., Yeremin, A. V.: Chemical characterization of element 112. Nature **447**, 72 (2007).
7. Gregorich, K. E., Henderson, R. A., Lee, D. M., Nurmia, M. J., Chasteler, R. M., Hall, H. L., Bennett, D. A., Gannett, C. M., Chadwick, R. B., Leyba, J. D., Hoffman, D. C., Herrmann, G.: Aqueous chemistry of element 105. Radiochim. Acta **43**, 223 (1988).
8. Kratz, J. V., Zimmermann, H. P., Scherer, U. W., Schädel, M., Brüchle, W., Gregorich, K. E., Gannett, C. M., Hall, H. L., Henderson, R. A., Lee, D. M., Leyba, J. D., Nurmia, M. J., Hoffman, D. C., Gäggeler, H., Jost, D., Baltensperger, U., Ya Nai-Qi, Türler, A., Lienert, Ch.: Chemical properties of element 105 in aqueous solution: Halide complex formation and anion exchange into triisooctyl amine. Radiochim. Acta **48**, 121 (1989).
9. Gober, M. K., Kratz, J. V., Zimmermann, H. P., Schädel, M., Brüchle, W., Schimpf, E., Gregorich, K. E., Türler, A., Hannink, N. J., Czerwinski, K. R., Kadkhodayan, B., Lee, D. M., Nurmia, M. J., Hoffman, D. C., Gäggeler, H., Jost, D., Kovács, J., Scherer, U. W., Weber, A.: Chemical properties of element 105 in aqueous solution: Extractions into diisobutylcarbinol. Radiochim. Acta **57**, 77 (1992).
10. Schädel, M., Brüchle, W., Schimpf, E., Zimmermann, H. P., Gober, M. K., Krtaz, J. V., Trautmann, N., Gäggeler, H., Jost, D., Kovács, J., Scherer, U. W., Weber, A., Gregorich, K. E., Türler, A., Czerwinski, K. R., Hannink, N. J., Kadkhodayan, B., Lee, D. M., Nurmia, M. J., Hoffman, D. C.: Chemical properties of element 105 in aqueous solution: Cation exchange separation with α-hydroxyisobutyric acid. Radiochim. Acta **57**, 85 (1992).
11. Zimmermann, H. P., Gober, M. K., Kratz, J. V., Schädel, M., Brüchle, W., Schimpf, E., Gregorich, K. E., Türler, A., Czerwinski, K. R., Hannink, N. J., Kadkhodayan, B., Lee, D. M., Nurmia, M. J., Hoffman, D. C., Gäggeler, H., Jost, D., Kovács, J. Scherer, U. W., Weber, A.: Chemical properties of element 105 in aqueous solution: back extraction from triisooctyl amine into 0.5 M HCl. Radiochim. Acta **60**, 11 (1993).
12. Paulus, W., Kratz, L. V., Strub, E., Zauner, S., Brüchle, W., Pershina, V., Schädel, M., Schausten, B., Adams, J. L., Gregorich, K. E., Hoffman, D. C., Lane, M. R., Laue, C., Lee, D. M., McGrath, C. A., Shaughnessy, D. K., Strellis, D. A., Sylwester, E. R.: Chemical properties of element 105 in aqueous solution: extraction of the fluoride-, chloride-, and bromide complexes of the group-5 elements into an aliphatic amine. Radiochim. Acta. **84**, 69 (1999).
13. Trubert, D., Naour, C. Le, Guzman, F. M., Hussonnois, M., Brillard, L., Le Du, J. F., Constantinescu, O., Gasparro, J., Barci, V., Weiss, B., Ardisson, G.: Chemical isolation of dubnium (element 105) in fluoride media. Radiochim. Acta **90**, 127 (2002).
14. Strub, E., Kratz, J. V., Kronenberg, A., Nähler, A., Thörle, P., Zauner, S., Brüchle, W., Jäger, E., Schädel, M., Schausten, B., Schimpf, E., Zongwei, Li, Kirbach, U., Schumann, D., Jost, D., Türler, A., Asai, M., Nagame, Y., Sakama, M., Tsukada, K., Gäggeler, H. W., Glatz, J. P.: Fluoride complexation of rutherfordium (Rf, Element 104). Radiochim. Acta **88**, 265 (2000).
15. Kronenberg, A., Eberhardt, K., Kratz, J. V., Mohapatra, P. K., Nähler, A., Thörle, P., Brüchle, W., Schädel, M., Türler, A.: On-line anion exchange of rutherfordium in HF/HNO_3 and HF solutions. Radiochim. Acta **92**, 379 (2004).
16. Haba, H., Tsukada, K., Asai, M., Toyoshima, A., Akiyama, K., Nishinaka, I., Hirata, M., Yaita, T., Ichikawa, S., Nagame, Y., Yasuda, K., Miyamoto, Y., Kaneko, T., Goto, S., Ono, S., Hirai, T., Kudo, H., Shigekawa, M., Shinohara, A., Oura, Y., Nakahara, H., Sueki, K., Kikunaga, H., Kinoshita, N., Tsuruga, N., Yokoyama, A., Sakama, M., Enomoto, S., Schädel, M., Brüchle, W., Kratz, J. V.: Fluoride complexation of element 104, rutherfordium. J. Am. Chem. Soc. **126**, 5219 (2004).
17. Toyoshima, A., Haba, H., Tsukada, K., Asai, M., Akiyama, K., Nishinaka, I., Nagame, Y., Saika, D., Matsuo, K., Sato, W., Shinohara, A., Ishizu, H., Ito, M., Saito, J., Goto, S., Kudo, H., Kikunaga, H., Kinoshita, N., Kato, C., Yokoyama, A., Sueki, K.: Elution curve of rutherfordium (Rf) in anion-exchange chromatography with hydrofluoric acid (HF) solution. J. Nucl. Radiochem. Sci. **5**, 45 (2004).
18. Toyoshima, A., Haba, H., Tsukada, K., Asai, M., Akiyama, K., Goto, S., Sato, W., Ishii, Y., Nishinaka, I., Sato, T. K., Nagame, Y., Tani, Y., Hasegawa, H., Matsuo, K., Saika, D., Kitamoto, Y., Shinohara, A., Ito, M., Saito, J., Kudo, H., Yokoyama, A., Sakama, M., Sueki, K., Oura, Y., Nakahara, H., Schädel, M., Brüchle, W., Kratz, J. V.: Hexafluoro complex of rutherfordium in mixed HF/HNO_3 solutions. Radiochim. Acta **96**, 125 (2008).
19. Ishii, Y., Toyoshima, A., Tsukada, K., Asai, M., Toume, H., Nishinaka, I., Nagame, Y., Miyashita, S., Mori, S., Suganuma, H., Haba, H., Sakamaki, M., Goto, S., Kudo, H., Akiyama, K., Oura, Y., Nakahara, H., Tashiro, Y., Shinohara, A., Schädel, M., Brüchle, W., Pershina, V., Kratz, J. V.: Fluoride complexation of element 104, rutherfordium (Rf), investigated by cation-exchange chromatography. Chem. Lett. **37**, 288 (2008).
20. Nagame, Y., Tsukada, K., Asai, M., Toyoshima, A., Akiyama, K., Ishii, Y., Kaneko-Sato, T., Hirata, M., Nishinaka, I., Ichikawa, S., Haba, H., Enomoto, S., Matsuo, K., Saika, D., Kitamoto, Y., Hasegawa, H., Tani, Y., Sato, W., Shinohara, A., Ito, M., Saito, J., Goto, S., Kudo, H., Kikunaga, H., Kinoshita, N., Yokoyama, A., Sueki, K., Oura, Y., Nakahara, H., Sakama, M., Schädel, M.,

Brüchle, W., Kratz, J. V.: Chemical studies on rutherfordium (Rf) at JAERI. Radiochim. Acta **93**, 519 (2005).
21. Kasamatsu, Y., Toyoshima, A., Toume, H., Tsukada, K., Haba, H., Nagame, Y.: Anion-exchange behavior of Nb, Ta, and Pa as homologues of Db in HF/HNO_3 solutions. J. Nucl. Radiochem. Sci. **8**, 69 (2007).
22. Schädel, M., Brüchle, W., Jäger, E., Schimpf, E., Kratz, J. V., Scherer, U. W., Zimmermann, H. P.: ARCA-II – a new apparatus for fast, repetitiveve HPLC separation. Radiochim. Acta **48**, 171 (1989).
23. Nagame, Y., Asai, M., Haba, H., Goto, S., Tsukada, K., Nishinaka, I., Nishio, K., Ichikawa, S., Sakama, M., Toyoshima, A., Akiyama, K., Nakahara, H., Schädel, M., Kratz, J. V., Gäggeler, H. W., Türler, A.: Production cross sections of ^{261}Rf and ^{262}Db in bombardments of ^{248}Cm with ^{18}O and ^{19}F ions. J. Nucl. Radiochem. Sci. **3**, 85 (2002), private communication.
24. Plaisance, M., Guillaumont, R.: Fluoro- et chlorofluoro-complexes de protactinium pentavalent. Radiochim. Acta **12**, 32 (1969).
25. Varga, L. P., Freund, H.: The formation constants of the tantalum fluoride system. I. Potentiometric and anion exchange studies – Evidence for species of coordination number nine. J. Phys. Chem. **66**, 21 (1962).
26. Keller, C.: Untersuchungen über das Verhalten von Niob, Tantal und Protactinium gegenüber Ionenaustauschern. Radiochim. Acta **1**, 147 (1963).
27. Kim, J. L., Lagally, H., Born, H.-J.: Ion exchange in aqueous and in aqueous-organic solvents. Part I. Anion-exchange behavior of Zr, Nb, Ta and Pa in aqueous HCl-HF and in HCl-organic solvent. Anal. Chim. Acta **64**, 29 (1973).
28. Caletka, R., Krivan, V.: Behavior of 18 elements in HF and $HF\text{-}NH_4F$ media on anion exchanger in various ionic forms. J. Radioanal. Nucl. Chem. **142**, 359 (1990).
29. Monroy-Guzman, F., Trubert, D., Brillard, L., Kim, J. B., Hussonnois, M., Constantinescu, O.: Adsorption of Zr, Hf, Nb, Ta and Pa on macroporous anion exchangers in HF medium. J. Radioanal. Nucl. Chem. **208**, 461 (1996).
30. Trubert, D., Monroy-Guzman, F., Le Naour, C., Brillard, L., Hussonnois, M., Constantinescu, O.: Behaviour of Zr, Hf, Nb, Ta and Pa on macroporous anion exchangers in chloride-fluoride media. Anal. Chim. Acta **374**, 149 (1998).
31. Myasoedov, B. F., Kirby, H. W., Tananaev, I. G.: Protactinium. In: *The Chemistry of the Actinides and Transactinide Elements*. 3rd Edn., Vol. 1 (Morss, L. R., Edelstein, N. M., Fuger, J., eds.), Springer, Dordrecht (2006), p. 161.
32. Keller Jr., O. L.: Identification of complex ions of niobium (V) in hydrofluoric acid solution by Raman and infrared spectroscopy. Inorg. Chem. **2**, 783 (1963).
33. Keller Jr., O. L., Chetham-Strode Jr., A.: A study by Raman spectroscopy of complex ions formed by tantalum (V) in the system $Ta(V)\text{-}HF\text{-}NH_4F\text{-}H_2O$. Inorg. Chem. **5**, 367 (1966).
34. Korkisch, J.: *Handbook of Ion Exchange Resins: Their Application to Inorganic and Analytical Chemistry*. CRC Press, Florida (1989).
35. Glückauf, E.: Theory of chromatography. Part 9. The "theoretical plate" concept in column separations. Trans. Faraday Soc. **51**, 34 (1955).
36. Firestone, R. B., Shirley, V. S.: *Table of Isotopes*. 8th Edn., John Wiley and Sons, New York (1996).
37. Brüchle, W.: Confidence intervals for experiments with background and small numbers of events. Radiochim. Acta **91**, 71 (2003).
38. Pershina, V., Bastug, T.: Solution chemistry of element 105 Part III: Hydrolysis and complex formation of Nb, Ta, Db and Pa in HF and HBr solutions. Radiochim. Acta **84**, 79 (1999).

DOI: 10.1007/s10967-007-7320-6 *Journal of Radioanalytical and Nuclear Chemistry, Vol. 279, No.2 (2009) 371–376*

Adsorption of Nb, Ta and Pa on anion-exchanger in HF and HF/HNO_3 solutions: Model experiments for the chemical study of Db

Y. Kasamatsu,[1]* A. Toyoshima,[1] H. Haba,[2] H. Toume,[1] K. Tsukada,[1] K. Akiyama,[3] T. Yoshimura,[4] Y. Nagame[1]

[1] *Advanced Science Research Center, Japan Atomic Energy Agency, Tokai, Ibaraki 319-1195, Japan*
[2] *Nishina Center for Accelerator Based Science, RIKEN, Wako, Saitama 351-0198, Japan*
[3] *Graduate School of Science and Engineering, Tokyo Metropolitan University, Hachioji, Tokyo 192-0397, Japan*
[4] *Graduate School of Science, Osaka University, Toyonaka, Osaka 560-0043, Japan*

(Received March 10, 2008)

Anion-exchange behavior of the group-5 elements, Nb and Ta, and their pseudo homologue Pa in HF and HF/HNO_3 solutions was investigated by a batch method to find suitable conditions for the anion-exchange experiment of element 105 (Dubnium, Db). We determined the distribution coefficients of those elements on the anion-exchange resin as a function of the F^- and NO_3^- concentrations. Clearly different anion-exchange behavior was observed among these elements. Based on the results, we discuss the fluoro-complex formation of each element and suggest experimental conditions for the study of fluoride complexation of Db.

Introduction

The transactinide elements with atomic numbers $Z \geq 104$ must be produced by accelerators using nuclear reactions of heavy-ion beams with heavy target materials. Chemical studies of such elements are conducted on a one-atom-at-a-time basis by rapid chemical separation techniques because of considerably low production rates and short half-lives of the transactinide nuclides.[1,2] Chemical experiments of the transactinide elements are often performed together with their lighter homologues to compare the properties with those of the homologues.

Several model experiments aiming at the chemical study of Dubnium (Db) in aqueous solution have been performed using the lighter homologues Nb and Ta, and the pseudo homologue Pa.[3–6] Some mutual separations of the group-5 homologues by chromatographic methods have been applied to the isolation of ^{262}Db ($T_{1/2}$ = 34 s) and ^{263}Db ($T_{1/2}$ = 27 s) produced in proper nuclear reactions, and the behavior of Db was compared with that of the homologues under each experimental condition.[7–14] For clear understanding of the chemical properties of Db, further systematic investigations are strongly required.

Chemical characterization of Db is also important to verify the synthesis of element 115.[15,16] A long-lived spontaneously fissioning nuclide which is one of the descendants of ^{288}Db (Z = 115) produced in the ^{243}Am(^{48}Ca, 3n) reaction was assigned to ^{268}Db or, after EC-decay, to ^{268}Rf (Z = 104).[16] To confirm the above assignment, the long-lived nuclides ^{268}Db/^{268}Rf have to be unequivocally identified by definite chemical isolations of Db and Rf; the chemical behavior of these elements should be established.

In our previous works, distribution coefficients (K_d) of Rf were successfully determined by the anion-exchange experiments in HF and HF/HNO_3 solutions with AIDA (Automated Ion-exchange separation apparatus coupled with the Detection system for Alpha-spectroscopy), and the results clearly showed that the fluoride complexation of Rf is significantly weaker than that of the homologues Zr and Hf.[17–19] Quite unique and unexpected behavior of Rf was observed in the fluoride complexation. As a subsequent step, we plan to investigate fluoride complexation of Db through anion-exchange experiments in HF/HNO_3; the K_d values of Db will be systematically measured as a function of the ligand (F^-) and the counter-ion (NO_3^-) concentrations as those with Rf.[18] The K_d values of Nb, Ta and Pa on the anion-exchange resin were previously determined as a function of the fluoride ion concentration ([F^-]) in HF/HNO_3 at [NO_3^-] = 0.1M.[20] In this work, variations of the K_d values of these elements were accurately measured as a function of [NO_3^-] for further discussion on the formation of anionic fluoro complexes of the group-5 elements. Based on the results, we propose suitable experimental conditions for the anion-exchange chromatography of Db.

Experimental

We used the radiotracers of ^{95}Nb, ^{177,179}Ta and ^{233}Pa to measure the K_d values on the anion-exchange resin. The experimental procedures are basically the same as those described in the previous report.[20]

* E-mail: kasamatsu.yoshitaka@jaea.go.jp

0236–5731/USD 20.00

Akadémiai Kiadó, Budapest
Springer, Dordrecht

The K_d value is obtained from a ratio of the radioactivity in the resin phase (A_r) to that in the solution (A_s) as:

$$K_d = \frac{A_r V_s}{A_s W_r} \quad (1)$$

where V_s is the volume of the solution (mL) and W_r the weight of the dry resin (g). In a polypropylene (PP) test tube, 8–200 mg of the dried anion-exchange resin MCI GEL CA08Y (particle size of 25 μm) and 3 mL of HF or HF/HNO_3 solution containing the radiotracers of ^{95}Nb, $^{177,179}Ta$ and ^{233}Pa were mixed. In each sample, the numbers of atoms of the radiotracers were 10^8–10^{12}. Then, the tube was shaken for 15 minutes. After centrifugation, 1 mL of the solution was pipetted into a small PP container and subjected to X- and γ-ray spectrometry with a Ge semiconductor detector. The same treatment was conducted without resin to monitor the reference radioactivity in each solution. The radioactivity in the resin phase was evaluated by subtracting that in the supernatant solution from the reference radioactivity. Only statistical errors were taken into account for the evaluation of errors in the K_d values. The K_d values of Nb, Ta and Pa on the anion-exchange resin in HF/HNO_3 solutions were determined as a function of $[NO_3^-]$ under the following conditions: the constant fluoride ion concentration $[F^-]=2.0\cdot10^{-4}$, $3.0\cdot10^{-3}$ and $1.0\cdot10^{-2}$ M. The K_d values in pure HF solutions ($[NO_3^-]=0$M) were also measured as a function of $[F^-]$ in the concentration range of $8.9\cdot10^{-3}$–$1.7\cdot10^{-2}$M (0.11–2.0M HF). The fluoride ion concentrations were calculated using the dissociation constants of HF and HF_2^- for equilibria expressed by the following chemical reactions (2) and (3), respectively:[21]

$$H^+ + F^- \rightleftarrows HF \quad (2)$$

$$HF + F^- \rightleftarrows HF_2^- \quad (3)$$

Results and discussion

Variations of the K_d values of Nb, Ta and Pa on the anion-exchange resin in HF/HNO_3 solutions are shown in Fig. 1 as a function of $[NO_3^-]$ at constant $[F^-]$ of (a) $2.0\cdot10^{-4}$, (b) $3.0\cdot10^{-3}$ and (c) $1.0\cdot10^{-2}$M. In the $\log K_d$ vs. $\log[NO_3^-]$ plot, $\log K_d$ linearly decreases with increasing $\log[NO_3^-]$ for every element. Thus, we fitted a linear expression to the data with the least squares fitting. The slopes of the fitted lines are presented in Table 1. In every concentration of $[F^-]$, the absolute values of the minus slopes are in the sequence of Pa>Nb>Ta. The present K_d values at $[NO_3^-]=0.1$M are in good agreement with those obtained in the previous study as depicted in Fig. 2. The K_d values obtained in HF solutions are also plotted in Fig. 2. It is obvious from the figure that the K_d values of the elements become small in HF/HNO_3 by the effect of the NO_3^- ions as a counter ion and that the differential between the K_d values in HF and those in HF/HNO_3 is the largest for Pa, which is consistent with the largest absolute value of the slope for Pa in Table 1.

On the assumption that consecutive coordination of the fluoride ion to metal cations proceeds in the formation of the anionic fluoro complexes or oxo-fluoro complexes with increasing $[F^-]$,[20] formation constants of the anionic complexes with –1 and –2 charges are given by:

$$K_6 = \frac{[MF_6^-]}{[MF_5][F^-]} \quad (4)$$

and

$$K_7 = \frac{[MF_7^{2-}]}{[MF_6^-][F^-]} \quad (5)$$

respectively, where M represents the pentavalent metal ion as M^{5+}. In the case of the oxo-fluoro complexes, MO^{3+} is substituted for MF_2^{3+}; for example, the complex MOF_4^- is replaced by MF_6^-.

Equilibrium constants of anion-exchange reactions, D_6 and D_7, with the resin are expressed by:

$$D_6 = \frac{[RMF_6][L^-]}{[MF_6^-][RL]} \quad (6)$$

$$D_7 = \frac{[R_2MF_7][L^-]^2}{[MF_7^{2-}][RL]^2} \quad (7)$$

where R and L^- represent the anion-exchange resin and a counter ion, respectively. Formation of the complex with a –3 charge and further charged anionic complexes are not taken into consideration because the complexes with the –1 and/or –2 charges are the dominant species in both the solution and the resin phase even in concentrated HF solutions for Nb and Ta, which has been verified from the EXAFS and Raman spectroscopic studies of these elements.[22,23]

Table 1. Slopes (s) of the fitted linear lines in Fig. 1: $\log K_d = s \log [NO_3^-] + C$

$[F^-]$, M	Slope (s)		
	Nb	Ta	Pa
$2.0\cdot10^{-4}$	–1.0 ± 0.1	–0.5 ± 0.1	–1.2 ± 0.1
$3.0\cdot10^{-3}$	–1.3 ± 0.1	–1.2 ± 0.1	–1.8 ± 0.1
$1.0\cdot10^{-2}$	–1.5 ± 0.1	–1.3 ± 0.1	–2.0 ± 0.1

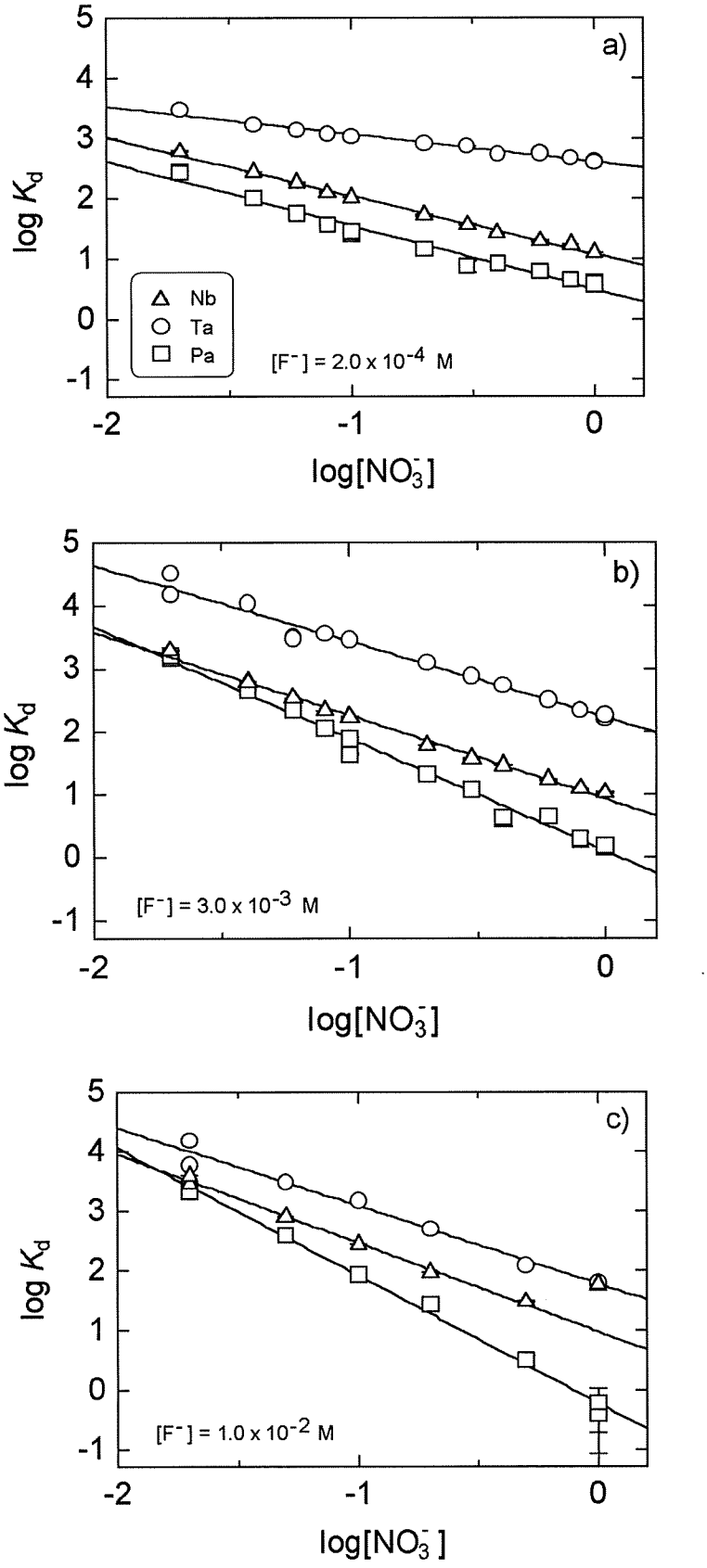

Fig. 1. Variations of the K_d values of ^{95}Nb, ^{179}Ta and ^{233}Pa on the anion-exchange resin as a function of [NO_3^-] at the constant [F^-] of (a) $2.0 \cdot 10^{-4}$, (b) $3.0 \cdot 10^{-3}$ and (c) $1.0 \cdot 10^{-2}$M

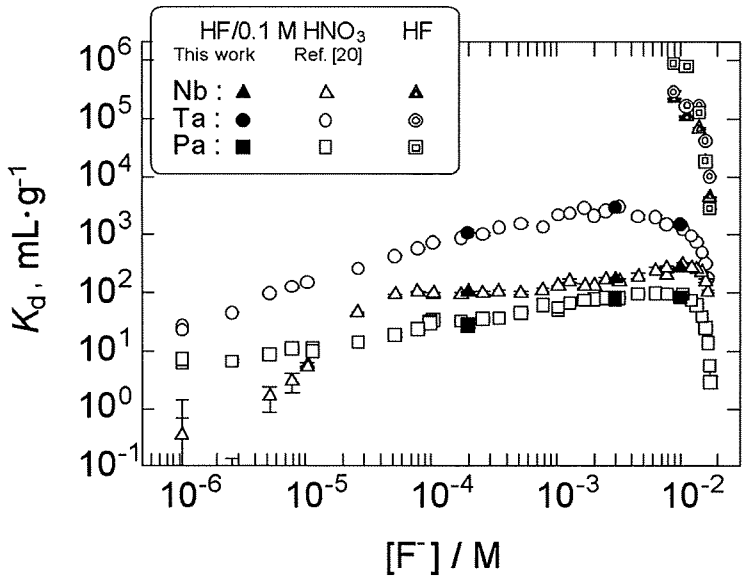

Fig. 2. Variations of the K_d values of Nb, Ta and Pa on the anion-exchange resin as a function of $[F^-]$ in HF/HNO_3 media (closed symbols) and in HF media (twofold symbols) together with those reported in Reference 20 (open symbols)

It is also reported that Pa forms the anionic fluoro complexes of PaF_6^- and/or PaF_7^{2-} except in the extremely concentrated HF solution.[24–26] The K_d values in the exchange reaction of the complexes of interest between the solution and the resin phase is described as:

$$K_d = \frac{[RMF_6]+[R_2MF_7]}{[MF_5]+[MF_6^-]+[MF_7^{2-}]} \tag{8}$$

From Eqs (4) to (7), the following expression is obtained:

$$K_d = \frac{[RL][L^-]K_6D_6[F^-]+[RL]^2K_6K_7D_7[F^-]^2}{[L^-]^2(1+K_6[F^-]+K_6K_7[F^-]^2)} \tag{9}$$

When only single species dominantly interacts with the resin, Eqs (10) and (11) are given for the species with the –1 and –2 charges, respectively:

$$\log K_d = -\log\frac{[L^-]}{[RL]} + \log K_6D_6 + \\ + \log\left(\frac{[F^-]}{1+K_6[F^-]+K_6K_7[F^-]^2}\right) \tag{10}$$

$$\log K_d = -2\log\frac{[L^-]}{[RL]} + \log K_6K_7D_7 + \\ + \log\left(\frac{[F^-]^2}{1+K_6[F^-]+K_6K_7[F^-]^2}\right) \tag{11}$$

The concentration of the counter ion in the resin phase, [RL], can be regarded as a constant value because it is equal to the exchange capacity of the resin phase. Since the contribution of F^- and HF_2^- as the counter ions is negligible at $[F^-]<5\cdot10^{-3}$M in HF/HNO_3 solutions,[18] $[L^-]$ can be replaced by $[NO_3^-]$ in such $[F^-]$ range. Thus, the slope of the linear fit in the $\log K_d$ vs. $\log[NO_3^-]$ plot at constant $[F^-]$ of $<5\cdot10^{-3}$M corresponds to the charge of the anionic complex which interacts with the resin. In this work, therefore, the charges of the complexes can be evaluated from the slopes under the following conditions, $[F^-]=2.0\cdot10^{-4}$ and $3.0\cdot10^{-3}$M (Figs 1a and 1b). The relationship between the slope and the electric charge of the complex ion holds even if the existences of the metal cation (M^{5+}) and other fluoro complexes such as MF^{4+} and MF_2^{3+} in the solution are taken into account.[18]

The absolute value of the minus slope in Table 1 becomes larger for every element with increasing $[F^-]$. This means that the coordination number of the fluoride ion to the metal cation increases with increasing $[F^-]$, indicating the consecutive formation of the fluoro complexes of the group-5 elements. The sequence of the absolute slope values for the elements mentioned above (Pa>Nb>Ta) corresponds to that of the charge number of the anionic complexes on the condition that $[F^-]=2.0\cdot10^{-4}$ and $3.0\cdot10^{-3}$M.

As for chemical species, it is reported that Ta and Pa form fluoro complexes MF_n^{5-n}, while Nb is dominantly present as oxo-fluoro complexes $NbOF_n^{3-n}$ in aqueous solutions containing fluoride ions with a wide range of $[F^-]$.[4–6,22–27] Especially, the EXAFS and Raman spectroscopic studies of Nb and Ta suggest that TaF_7^{2-} and $NbOF_5^{2-}$ are the dominant species in 0.1–10M HF solutions ($[F^-]=8.9\cdot10^{-3}$–$1.9\cdot10^{-2}$M).[22,23]

From the present results, it is deduced that Nb forms the anionic complex $NbOF_4^-$ which interacts with the anion-exchange resin at the diluted $[F^-]$, whereas $NbOF_5^{2-}$ would coexists at $[F^-]=3.0\cdot10^{-3}$M. Tantalum would form the TaF_6^- complex at $[F^-]$ of $3.0\cdot10^{-3}$M. From the slope of –0.5 at $[F^-]=2.0\cdot10^{-4}$M in Table 1, it would be possible to interpret that hydrolysis species of Ta are present at such dilute F^- concentration. Actually hydrolysis species is reported to dominate the fluoride complexation of Ta at $[F^-]$ lower than $1\cdot10^{-3}$M.[5] PaF_6^- and PaF_7^{2-} are considered to be formed at $[F^-]$ of $2.0\cdot10^{-4}$ and $3.0\cdot10^{-3}$M, respectively.

Regardless of the clear difference in chemical species between Nb and Ta, the variations of the K_d values of Nb and Ta as a function of $[F^-]$ as well as the absolute values of the K_d values are quite similar with each other in HF solutions under the studied conditions as shown in Fig. 2. On the other hand, in HF/HNO_3, the K_d values of Nb are quite different from those of Ta, and a unique variation of the K_d values of Nb against $[F^-]$ is observed,[20] probably reflecting its uniqueness of the chemical species. To discuss the fluoride complexation of the group-5 elements including Db, a systematic anion-exchange study of Db in HF/HNO_3 is indispensable. The K_d values of Db should be determined in a wide range of $[F^-]$ to observe consecutive formation of the fluoro complexes. The variation of the K_d values as a function of $[NO_3^-]$ should be also measured in the concentration range of $[F^-]<5\cdot10^{-3}$M to evaluate the charge number of the complex of Db without the influence of the other counter ions.

Conclusions

The K_d values of Nb, Ta and Pa on the anion-exchange resin were determined as a function of $[NO_3^-]$, and clearly different anion-exchange behavior was observed among the elements in HF/HNO_3 solutions. Analysis of the slopes of the linear fittings in the $\log K_d$ vs. $\log[NO_3^-]$ plot enables us to evaluate the charges of the anionic fluoro complexes of the group-5 elements. Their chemical species were deduced based on the knowledge in the references as follows: (1) $NbOF_4^-$ would be present at $[F^-]=2.0\cdot10^{-4}$ and $3.0\cdot10^{-3}$M, (2) TaF_6^- seems to be dominantly present at $[F^-]=3\cdot10^{-3}$M and Ta is hydrolyzed at $[F^-]=2.0\cdot10^{-4}$M, and (3) PaF_6^- and PaF_7^{2-} would be dominantly present at $[F^-]=2.0\cdot10^{-4}$ and $3.0\cdot10^{-3}$M, respectively.

*

The authors thank the staffs of the RIKEN Accelerator Research Facility for the productions of ^{95}Nb and ^{179}Ta.

References

1. M. SCHÄDEL, Angew. Chem. Intern. Ed., 45 (2006) 368.
2. J. V. KRATZ, Pure Appl. Chem., 75 (2003) 103.
3. M. SCHÄDEL, W. BRÜCHLE, E. JÄGER, E. SCHIMPF, J. V. KRATZ, U. W. SCHERER, H. P. ZIMMERMANN, Radiochim. Acta, 48 (1989) 171.
4. F. MONROY GUZMAN, D. TRUBERT, L. BRILLARD, J. B. KIM, M. HUSSONNOIS, O. CONSTANTINESCU, J. Radioanal. Nucl. Chem., 208 (1996) 461.
5. D. SCHUMANN, S. FISCHER, R. DRESSLER, ST. TAUT, H. NITSCHE, N. TRAUTMANN, M. SCHÄDEL, W. BRÜCHLE, B. SCHAUSTEN, A. F. NOVGORODOV, R. MISIAK, B. EICHLER, H. GÄGGELER, D. JOST, A. TÜRLER, H. BRUCHERTSEIFER, Radiochim. Acta, 72 (1996) 137.
6. D. TRUBERT, F. MONROY GUZMAN, C. LE NAOUR, L. BRILLARD, M. HUSSONNOIS, O. CONSTANTINESCU, Anal. Chim. Acta, 374 (1998) 149.
7. K. E. GREGORICH, R. A. HENDERSON, D. M. LEE, M. J. NURMIA, R. M. CHASTELER, H. L. HALL, D. A. BENNETT, C. M. GANNETT, R. B. CHADWICK, J. D. LEYBA, D. C. HOFFMAN, G. HERRMANN, Radiochim. Acta, 43 (1988) 223.
8. J. V. KRATZ, H. P. ZIMMERMANN, U. W. SCHERER, M. SCHÄDEL, W. BRÜCHLE, K. E. GREGORICH, C. M. GANNETT, H. L. HALL, R. A. HENDERSON, D. M. LEE, J. D. LEYBA, M. J. NURMIA, D. C. HOFFMAN, H. GÄGGELER, D. JOST, U. BALTENSPERGER, YA NAI-QI, A. TÜRLER, CH. LIENERT, Radiochim. Acta, 48 (1989) 121.
9. M. K. GOBER, J. V. KRATZ, H. P. ZIMMERMANN, M. SCHÄDEL, W. BRÜCHLE, E. SCHIMPF, K. E. GREGORICH, A. TÜRLER, N. J. HANNINK, K. R. CZERWINSKI, B. KADKHODAYAN, D. M. LEE, M. J. NURMIA, D. C. HOFFMAN, H. GÄGGELER, D. JOST, J. KOVACS, U. W. SCHERER, A. WEBER, Radiochim. Acta, 57 (1992) 77.
10. M. SCHÄDEL, W. BRÜCHLE, E. SCHIMPF, H. P. ZIMMERMANN, M. K. GOBER, J. V. KRATZ, N. TRAUTMANN, H. GÄGGELER, D. JOST, J. KOVACS, U. W. SCHERER, A. WEBER, K. E. GREGORICH, A. TÜRLER, K. R. CZERWINSKI, N. J. HANNINK, B. KADKHODAYAN, D. M. LEE, M. J. NURMIA, D. C. HOFFMAN, Radiochim. Acta, 57 (1992) 85.
11. H. P. ZIMMERMANN, M. K. GOBER, J. V. KRATZ, M. SCHÄDEL, W. BRÜCHLE, E. SCHIMPF, K. E. GREGORICH, A. TÜRLER, K. R. CZERWINSKI, N. J. HANNINK, B. KADKHODAYAN, D. M. LEE, M. J. NURMIA, D. C. HOFFMAN, H. GÄGGELER, D. JOST, J. KOVACS, U. W. SCHERER, A. WEBER, Radiochim. Acta, 60 (1993) 11.
12. W. PAULUS, J. V. KRATZ, E. STRUB, S. ZAUNER, W. BRÜCHLE, V. PERSHINA, M. SCHÄDEL, B. SCHAUSTEN, J. L. ADAMS, K. E. GREGORICH, D. C. HOFFMAN, M. R. LANE, C. LAUE, D. M. LEE, C. A. MCGRATH, D. K. SHAUGHNESSY, D. A. STRELLIS, E. R. SYLWESTER, J. Alloys Comp., 271–273 (1998) 292.
13. W. PAULUS, J. V. KRATZ, E. STRUB, S. ZAUNER, W. BRÜCHLE, V. PERSHINA, M. SCHÄDEL, B. SCHAUSTEN, J. L. ADAMS, K. E. GREGORICH, D. C. HOFFMAN, M. R. LANE, C. LAUE, D. M. LEE, C. A. MCGRATH, D. K. SHAUGHNESSY, D. A. STRELLIS, E. R. SYLWESTER, Radiochim. Acta, 84 (1999) 69.
14. Y. NAGAME, H. HABA, K. TSUKADA, M. ASAI, A. TOYOSHIMA, S. GOTO, K. AKIYAMA, T. KANEKO, M. SAKAMA, M. HIRATA, T. YAITA, I. NISHINAKA, S. ICHIKAWA, H. NAKAHARA, Nucl. Phys., A734 (2004) 124.

15. YU. TS. OGANESSIAN, V. K. UTYONKOV, S. N. DMITRIEV, YU. V. LOBANOV, M. G. ITKIS, A. N. POLYAKOV, YU. S. TSYGANOV, A. N. MEZENTSEV, A. V. YEREMIN, A. A. VOINOV, E. A. SOKOL, G. G. GULBEKIAN, S. L. BOGOMOLOV, S. ILIEV, V. G. SUBBOTIN, A. M. SUKHOV, G. V. BUKLANOV, S. V. SHISHKIN, V. I. CHEPYGIN, G. K. VOSTOKIN, N. V. AKSENOV, M. HUSSONNOIS, K. SUBOTIC, V. I. ZAGREBAEV, K. J. MOODY, J. B. PATIN, J. F. WILD, M. A. STOYER, N. J. STOYER, D. A. SHAUGHNESSY, J. M. KENNEALLY, P. A. WILK, R. W. LOUGHEED, H. W. GÄGGELER, D. SCHUMANN, H. BRUCHERTSEIFER, R. EICHLER, Phys. Rev., C72 (2005) 034611.
16. D. SCHUMANN, H. BRUCHERTSEIFER, R. EICHLER, B. EICHLER, H. W. GÄGGELER, S. N. DMITRIEV, YU. TS. OGANESSIAN, V. K. UTYONKOV, S. V. SHISHKIN, A. V. YEREMIN, YU. V. LOBANOV, Y. S. TSYGANOV, V. I. CHEPYGIN, E. A. SOKOL, G. K. VOSTOKIN, N. V. AKSENOV, M. HUSSONNOIS, M. G. ITKIS, Radiochim. Acta, 93 (2005) 727.
17. H. HABA, K. TSUKADA, M. ASAI, A. TOYOSHIMA, K. AKIYAMA, I. NISHINAKA, M. HIRATA, T. YAITA, S. ICHIKAWA, Y. NAGAME, K. YASUDA, Y. MIYAMOTO, T. KANEKO, S. GOTO, S. ONO, T. HIRAI, H. KUDO, M. SHIGEKAWA, A. SHINOHARA, Y. OURA, H. NAKAHARA, K. SUEKI, H. KIKUNAGA, N. KINOSHITA, N. TSURUGA, A. YOKOYAMA, M. SAKAMA, S. ENOMOTO, M. SCHÄDEL, W. BRÜCHLE, J. V. KRATZ, J. Am. Chem. Soc., 126 (2004) 5219.
18. A. TOYOSHIMA, H. HABA, K. TSUKADA, M. ASAI, K. AKIYAMA, S. GOTO, Y. ISHII, I. NISHINAKA, T. K. SATO, Y. NAGAME, W. SATO, Y. TANI, H. HASEGAWA, K. MATSUO, D. SAIKA, Y. KITAMOTO, A. SHINOHARA, M. ITO, J. SAITO, H. KUDO, A. YOKOYAMA, M. SAKAMA, K. SUEKI, Y. OURA, H. NAKAHARA, M. SCHÄDEL, W. BRÜCHLE, J. V. KRATZ, Radiochim. Acta, in press.
19. Y. NAGAME, K. TSUKADA, M. ASAI, A. TOYOSHIMA, K. AKIYAMA, Y. ISHII, T. KANEKO-SATO, M. HIRATA, I. NISHINAKA, S. ICHIKAWA, H. HABA, S. ENOMOTO, K. MATSUO, D. SAIKA, Y. KITAMOTO, H. HASEGAWA, Y. TANI, W. SATO, A. SHINOHARA, M. ITO, J. SAITO, S. GOTO, H. KUDO, H. KIKUNAGA, N. KINOSHITA, A. YOKOYAMA, K. SUEKI, Y. OURA, H. NAKAHARA, M. SAKAMA, M. SCHÄDEL, W. BRÜCHLE, J. V. KRATZ, Radiochim. Acta, 93 (2005) 519.
20. Y. KASAMATSU, A. TOYOSHIMA, H. TOUME, K. TSUKADA, H. HABA, Y. NAGAME, J. Nucl. Radiochem. Sci., 8 (2007) 69.
21. M. PLAISANCE, R. GUILLAUMONT, Radiochim. Acta, 12 (1969) 32.
22. K. AKIYAMA et al., to be submitted.
23. O. L. KELLER, A. CHETHAN-STRODE, Inorg. Chem., 5 (1966) 367.
24. M. N. BUKHSH, J. FLEGENHEIMER, F. M. HALL, A. G. MADDOCK, C. F. MIRANDA, J. Inorg. Nucl. Chem., 28 (1966) 421.
25. J. I. KIM, H. LAGALLY, H. J. BORN, Anal. Chim. Acta, 64 (1973) 29.
26. B. F. MYASOEDOV, H. W. KIRBY, I. G. TANANAEV, Protactinium, in: The Chemistry of the Actinide and Transactinide Elements, Vol. 1, L. R. MORSS, N. M. EDELSTEIN, J. FUGER (Eds), 3rd ed., Springer, Dordrecht, The Netherlands, 2006, p. 213.
27. R. CALETKA, V. KRIVAN, J. Radioanal. Nucl. Chem., 142 (1990) 359.

Pure Appl. Chem., Vol. 80, No. 12, pp. 2657–2666, 2008.
doi:10.1351/pac200880122657

Development of multielemental imaging on semiconductor Compton telescope*

Shinji Motomura[1], Yousuke Kanayama[1,2], Hiromitsu Haba[1,2], Kaori Igarashi[2], Yasuyoshi Watanabe[1], and Shuichi Enomoto[1,2,‡]

[1]Molecular Imaging Research Program, RIKEN, 6-7-3 Minatojima-minamimachi, Chuo-ku, Kobe, Hyogo 650-0047, Japan; [2]Metallomics Research Unit, RIKEN, 2-1 Hirosawa, Wako, Saitama, 351-0198, Japan

Abstract: The feasibility of using a Compton camera for multitracer imaging has been demonstrated with the results of two biological sample imaging experiments. The distribution of the multitracer administered to a soybean sample and a tumor-bearing mouse has been visualized for each nuclide simultaneously. 3D images of the multitracer have been obtained even though the samples were measured from a fixed direction.

Keywords: Compton; Compton telescope; molecular imaging; multitracer imaging; Compton camera.

INTRODUCTION

The multitracer technique, which was invented at RIKEN in 1991 [1,2], is a powerful tool for investigating the behavior of various chemical elements in a sample. It is produced by irradiating a metal target with a heavy-ion beam accelerated to an energy of 135 MeV/u, and then by chemically processing the various radioactive nuclides produced mainly through nuclear-fragmentation reaction, into the final form such as multitracer solution. Since the multitracer contains the radioisotopes of various elements, the information regarding the radioisotopes under the same conditions can be obtained simultaneously by a single experiment. Moreover, the multitracer enables us to observe the correlated behavior among many elements. This information can never be obtained by combining the data of many single-tracer experiments. Owing to these advantages, the multitracer has found many applications in biology, medicine, environmental science, and other fields [3].

Although the potential advantages of multitracers are promising, no nondestructive inspection method has yet been established to realize their full potential particularly for in vivo imaging. This is because the multiple γ-rays emitted from the multitracer span an energy range from ~100 to 2 MeV. For energies above ~300 keV, sufficient spatial resolution cannot be obtained by a conventional γ-ray imager equipped with mechanical collimators. In addition, the energy resolution must be high enough to distinguish each nuclide contained in the multitracer.

In this paper, we describe a prototype of a Compton camera for multitracer imaging, which we call GREI (gamma-ray emission imaging), and present some results of test experiments with biological samples. The original idea of the Compton camera was invented in the early 1970s [4], and it was soon

*Paper based on a presentation at the International Symposium on Metallomics 2007 (ISM 2007), 28 November–1 December 2007, Nagoya, Japan. Other presentations are published in this issue, pp. 2565–2750.

‡Corresponding author

proposed for medical imaging [5]. Since then, various types of Compton camera have been proposed for various uses [6].

Previously, we performed a test experiment using a Compton camera composed of two segmented germanium (Ge) detectors [7]. Owing to the excellent energy resolution of the Ge detectors, three γ-ray sources of ^{60}Co, ^{137}Cs, and ^{152}Eu were clearly distinguished by setting energy windows on the corresponding γ-ray photo peaks, and their positions were simultaneously determined. The GREI system described in this paper has been modified taking into account the results of the test experiment, further simulations [8], and recent technologies developed for γ-ray detection [9–14].

DESCRIPTION OF THE GREI SYSTEM

The GREI system is composed of two double-sided orthogonal-strip Ge detectors manufactured by Eurisys Mesures (Fig. 1). The detectors are arranged parallel to each other and mounted in a single cryostat. The dimensions of the active volume of the Ge crystals are 39 × 39 × 10 mm and 39 × 39 × 20 mm for the front and rear detectors, respectively. The strip pitch is 3 mm for both detectors. The center-to-center distance between the crystals is 60 mm.

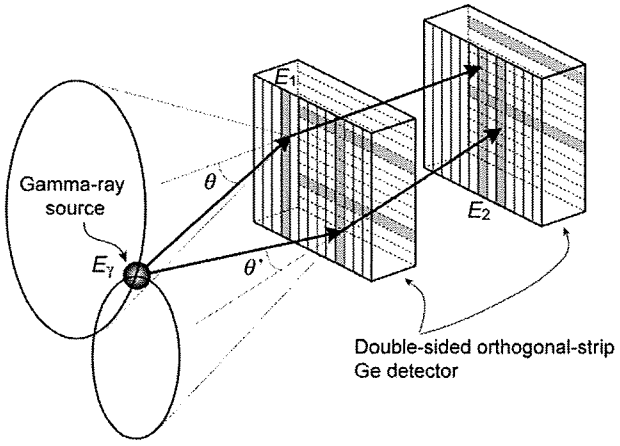

Fig. 1 Schematic of the strip Ge telescope operated as a Compton camera.

The electronics are schematically shown in Fig. 2. Conventional circuit modules based on nuclear instrument module (NIM) and computer automated measurement and control (CAMAC) standards are used. All the output signals of the preamplifiers are fed into the constant fraction discriminators (CFDs) through the timing filter amplifiers (TFAs), and the timing pulses are generated. All the timing pulses are fed into the time-to-digital converters (TDCs) to digitize the timing signals. To select the Compton scattering events, the timing pulses derived from the cathode strips are used to perform coincidence measurement between the front and rear detectors.

All the output signals of the preamplifiers are also fed into the shaping amplifiers to generate slow signals for energy measurement. Then the pulse heights are digitized by the analog-to-digital converters (ADCs).

In the current implementation, the transverse position of the γ-ray interaction is determined by a combination of the anode and cathode strips with the accuracy given by the width of the strip. On the other hand, the depth position of the γ-ray interaction in the Ge crystal can be determined more accurately than the thickness of the crystal, by taking into account the time difference between the signals from the anode and cathode strips [9–14]. To realize accurate depth measurement, the time constants of TFAs were set to 500 and 60 ns for differentiation and integration, respectively. Delay time

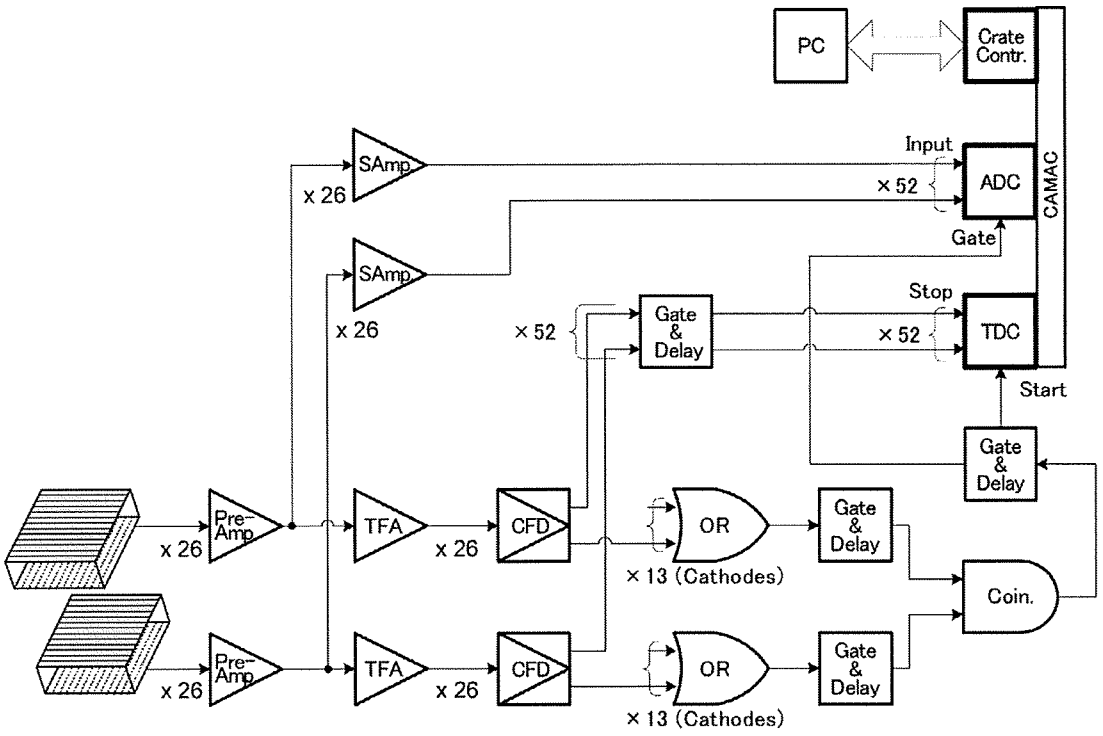

Fig. 2 Circuit diagram of the current prototype of the GREI system. The circuit modules are based on NIM and CAMAC standards.

of the CFDs was set to 50 ns, which was the upper limit of the modules, and the fraction of the CFDs was set to 0.5.

The digitized data of the TDCs and ADCs are transferred event by event to the personal computer. The transferred data are analyzed on-line, and also recorded in list mode for further off-line analysis. If an incident γ-ray is Compton scattered in the front detector and deposits energy E_1, and then the scattered γ-ray is fully absorbed in the rear detector and deposits energy E_2, the original γ-ray energy E_γ is obtained by summing E_1 and E_2. Thus, the nuclides contained in the multitracer are distinguished by setting energy windows at the corresponding energy peaks in the E_γ spectrum. Throughout this paper, the range of an energy window was ±5 keV of the peak position and the windows were applied in the software.

IMPLEMENTATION OF IMAGE RECONSTRUCTION METHODS

For image reconstruction, we are currently employing a two-step method. In the first step, an intermediate image, which is called a simple back-projection (SBP) image, is constructed by simply accumulating the back-projections over all detected events, using an algorithm analogous to the cone-surface mapping algorithm [15]. The back-projection for one event is a cone surface that indicates the possible position of the γ-ray source. The cone axis is the straight line passing through the first and second interaction points. The half-cone angle θ is the Compton scattering angle determined by the following equation:

$$\cos\theta = 1 + m_e c^2 \left(\frac{1}{E_\gamma} - \frac{1}{E_\gamma - E_1} \right) \tag{1}$$

where $m_e c^2$ is the rest-mass energy of an electron.

Here, we adopt a model that the SBP image is constructed by linear mapping of the source distribution image; that is,

$$n_i = \sum_j p_{ij} \lambda_j \tag{2}$$

where n_i is the value of voxel i in the SBP image, λ_j is the value of voxel j in the source distribution image, p_{ij} is the point-spread function (PSF), or the point kernel function [15], which represents the SBP image of the point source at voxel j; the 3D coordinates are represented by the single indices i and j. In general, the shape of the PSF varies depending on the source position, because the range of the accepted incident angle and scattering angle of γ-rays depends on the source position. Therefore, a spatially variant PSF must be used to perform rigorous image reconstruction. However, the PSF should be approximated by a spatially invariant PSF within a local region.

Then the second step is to deconvolve the SBP image with the PSF. We have implemented an analytical algorithm and an iterative algorithm for the deconvolution.

If the PSF is assumed to be spatially invariant, λ_j can be reconstructed analytically by adopting the Fourier convolution theorem. The matrix p_{ij} is diagonalized by taking the Fourier transform of both sides of eq. 2, and then λ_j is obtained in the spatial frequency domain as follows:

$$\lambda_j = \frac{n_j}{p_{jj}} \tag{3}$$

In most cases, an additional filter function (w_j) must be multiplied to the right side of eq. 3 in order to suppress the statistical noise components, which are dominant in the high-frequency regions, that is

$$\lambda_j = \frac{w_j n_j}{p_{jj}} \tag{4}$$

If a Wiener filter function can be designed for the system, eq. 4 becomes the optimal estimation in terms of the least square errors. In addition, ad hoc filter functions, such as a Butterworth function, can be used for w_j to suppress the noise components in the high-frequency regions.

We have also implemented an iterative deconvolution algorithm, which was adapted from the additive simultaneous reconstruction technique (SIRT) algorithm [16]. First, an initial estimate of the original image $\lambda_j^{(0)}$ is obtained by averaging the SBP image

$$\lambda_j^{(0)} = \frac{1}{N} \sum_{i=1}^{N} n_i \tag{5}$$

Then the $(n + 1)$-th estimate ($\lambda_j^{(n+1)}$) is obtained from the n-th estimate ($\lambda_j^{(n)}$) as follows:

$$\lambda_j^{(n+1)} = \lambda_j^{(n)} + \sum_i \left(n_i - \sum_k \lambda_k^{(n)} p_{ik} \right) p_{ij} \tag{6}$$

Although spatially variant PSFs can be used for p_{ij}, spatially invariant PSFs have been used in the current work.

A close examination shows that eq. 6 is the iteration term that minimizes the square errors of the SBP image constructed from the estimated source distribution. This can be seen if we recast the steepest descent iteration term from [17].

$$\begin{aligned}\Delta\lambda_j^{(n)} &= -\varepsilon\nabla\chi^2(\lambda_j^{(n)}) \\ &= -\varepsilon\frac{\sum_i \partial\left(n_i - \sum_k \lambda_k^{(n)} p_{ik}\right)^2}{\partial\lambda_j^{(n)}} \\ &= 2\varepsilon\sum_i\left(n_i - \sum_k \lambda_k^{(n)} p_{ik}\right)p_{ij}\end{aligned} \tag{7}$$

where $\Delta\lambda_j^{(n)}$ is the displacement of the estimate in the iteration step, ε is a positive coefficient used to control the iteration. When $\varepsilon = 0.5$, the second term on the right-hand side of eq. 6 is obtained.

Since the PSF has a 3D distribution, 3D deconvolution must be performed in order to reconstruct 3D images. However, when the source distribution can be considered to be 2D, corresponding to the case of a sliced sample, 2D deconvolution is sufficient because there is no contamination from outside of the 2D plane. Thus, we have implemented both 2D and 3D deconvolution algorithms.

PERFORMANCE OF THE PROTOTYPE

The absolute efficiencies for obtaining the full-energy γ-ray peaks from the sources 15 mm away from the center of the front detector are shown in Fig. 3, together with the values estimated by Monte Carlo simulation using a GEANT (GEometry ANd Tracking) [18] code. The experimental values were derived from the experimental data mentioned in the next section. One can see that the GREI system has significant efficiency between the energy range from ~200 keV to ~2 MeV.

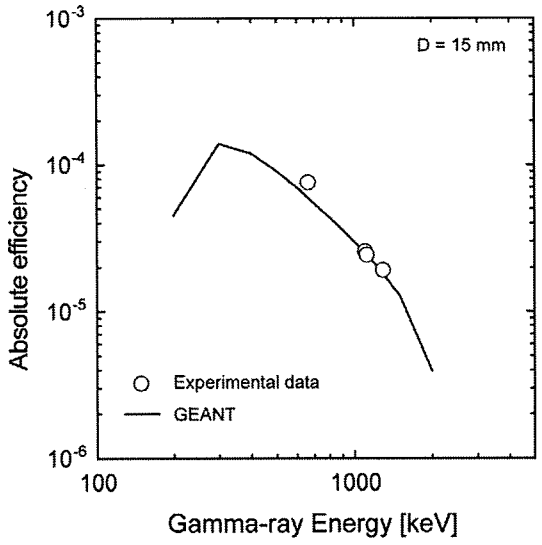

Fig. 3 Absolute efficiencies for obtaining the full-energy γ-ray peaks. The solid line indicates the numerical values calculated with a Monte Carlo simulation code GEANT [18].

The effect of the statistical noise on the spatial resolution achieved with the prototype system was investigated in terms of the Fourier power spectral density (FPSD) of the SBP image. A point-like source of ^{65}Zn, which emits 1116 keV γ-rays, was placed 69 mm away from the center of the front detector, and then three SBP images were constructed in 3D space with the detected event numbers of 1.0×10^4, 5.0×10^4, and 1.0×10^5. Then the SBP images were analytically deconvolved with the PSF constructed using a GEANT code. The full widths at half maximum (FWHMs) of the reconstructed images of the point source are shown in Table 1 for each number of events.

Table 1 Spatial resolution of the reconstructed image in FWHM, and derived transient spatial frequency (f_c) of the FPSD of the SBP image, where the statistical noise components are beginning to dominate. These values were determined for three different numbers of detected Compton scattering events.

Number of events	FWHM [mm]		f_c [mm^{-1}]	
	x-direction	z-direction	x-direction	z-direction
1.0×10^5	4.9	11.4	0.16 ± 0.02	0.06 ± 0.01
5.0×10^4	6.0	12.9	0.15 ± 0.02	0.05 ± 0.01
1.0×10^4	10.3	14.2	0.12 ± 0.03	0.04 ± 0.01

Experiment with biological samples

We have performed experiments with two biological samples in order to demonstrate the capability of nondestructive imaging of a multitracer. The first sample was a soybean plant administered with 310-kBq ^{137}Cs, 89-kBq ^{59}Fe, and 20-kBq ^{65}Zn. A photograph of the sample is shown in Fig. 6. The sample was fixed on a plane 15 mm away from the center of the front Ge detector. The measurement was carried out for 25 h.

Figure 4 shows the results of 2D imaging of the soybean sample. The energy windows were set at each peak position indicated in the γ-ray energy spectrum (Fig. 4a) to distinguish the radionuclides of ^{137}Cs, ^{59}Fe, and ^{65}Zn. The 2D SBP images were constructed for each nuclide on the plane where the sample was fixed, assuming a 2D distribution, and then the analytical reconstruction method was used to deconvolve the 2D SBP images with the 2D PSFs. The resulting images successfully visualized the different behaviors of the nuclides. The ^{137}Cs nuclide was distributed throughout the whole of the sample, because it is chemically analogous to K, while ^{59}Fe and ^{65}Zn remained near the root. The ^{65}Zn nuclide was found at the tip of the stem to some extent, where the plant was actively growing, because Zn is required for cell division.

In addition, we note that there is a difference in the background structure of the images. This is due to the difference in the number of events obtained for each nuclide; 2.5×10^6, 3.4×10^5, and 7.3×10^4 for ^{137}Cs, ^{59}Fe, and ^{65}Zn, respectively. The smaller the number of events, the larger the statistical noise component becomes.

The second sample was a tumor-bearing mouse administered intravenously with a multitracer solution that includes 60-kBq ^{65}Zn, 30-kBq ^{59}Fe, and 10-kBq ^{88}Y. The sample was fixed on a board and placed just under the front detector, which was installed with its front face down. The measurement was carried out for 95 h.

Figure 5 shows the results of 2D imaging of the tumor-bearing mouse. As in the case of the soybean sample, the energy windows were set at each peak position indicated in the γ-ray energy spectrum (Fig. 8a) to distinguish the radionuclides of ^{65}Zn, ^{59}Fe, and ^{88}Y. Then the 2D SBP images were constructed for each nuclide on the 2D plane that intersects the tumor part, and the SBP images were analytically deconvolved with the 2D PSFs. The resulting images are only "focused" images along the assumed plane, because the other parts of the sample have some contribution to the constructed 2D SBP

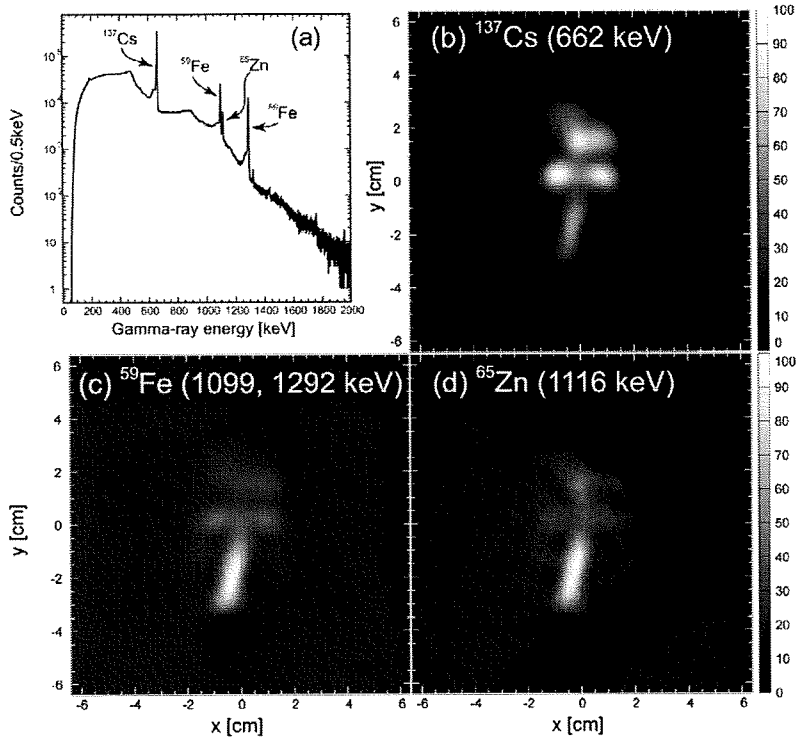

Fig. 4 Results of 2D imaging of the soybean sample.

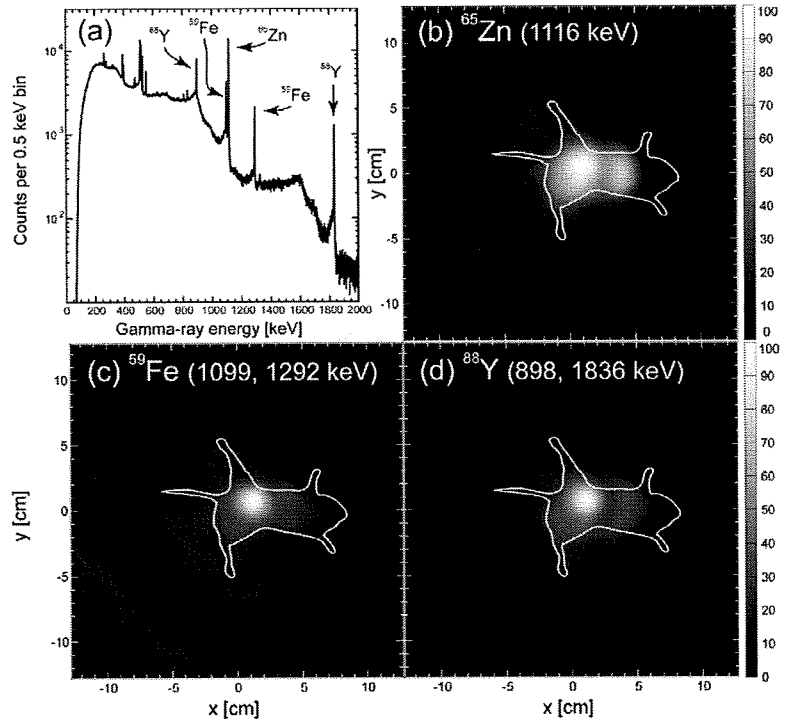

Fig. 5 Results of 2D imaging of the tumor-bearing mouse.

images. Nevertheless, the accumulation of the nuclides in the tumor site was evident and ^{65}Zn was also found in the liver. The results are consistent with those reported in [19–21].

We have performed 3D imaging of these samples, even though the samples were measured from a fixed direction. When the sample is sufficiently close to the front detector, the source distribution can be projected toward various directions because no mechanical collimator is used. This is a distinctive feature of a Compton camera. First, the 3D SBP images were constructed in 3D space, then the SBP images were deconvolved with the 3D PSFs.

Figure 6 shows the result of 3D imaging of ^{137}Cs in the soybean sample. The deconvolution was performed analytically. Since ^{137}Cs was distributed throughout the whole sample, the shape of the sample can be recognized. However, there exists a warp in the reconstructed image, which may have been caused by the use of spatially invariant PSFs.

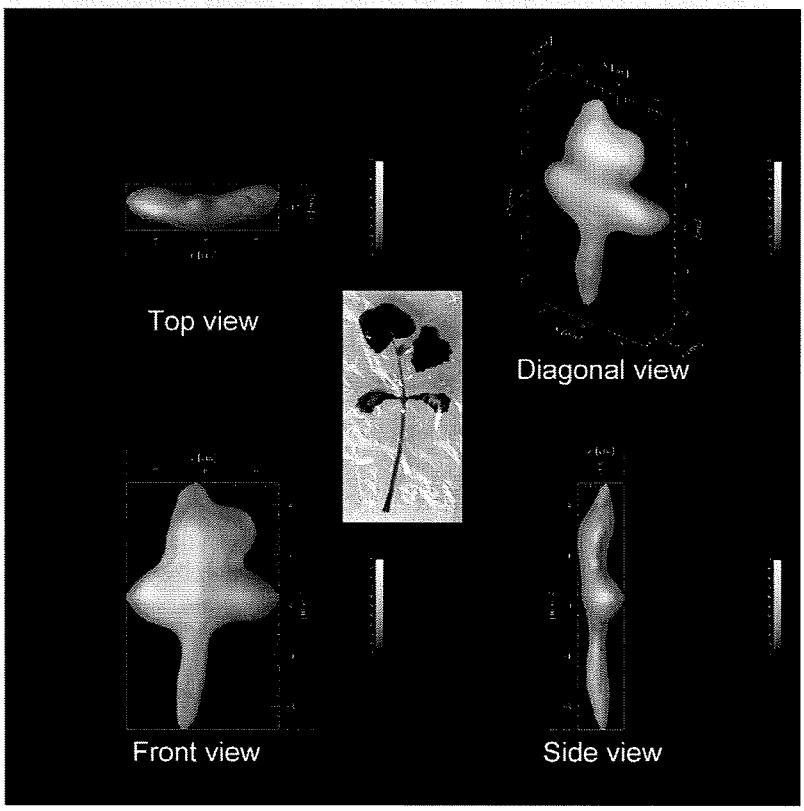

Fig. 6 Three-dimensional image of ^{137}Cs distributed in the soybean sample. A photograph of the sample is also shown at the center.

Figure 7 shows the result of 3D imaging of ^{65}Zn in the tumor-bearing mouse. In this case, we could not obtain any satisfactory images by analytical deconvolution. Thus, the reconstructed space was limited to only the region around the sample, and the iterative deconvolution was performed. The resulting image successfully visualized the accumulation of ^{65}Zn in the tumor and the liver. However, the image has a similar warp to the 3D image of the soybean sample. Spatially variant PSFs should be incorporated to obtain more accurate images.

We were able to demonstrate the feasibility of using the GREI system for nondestructive imaging of multitracer. Recently, we were succeeded in imaging dynamic metabolic processes of three radio-

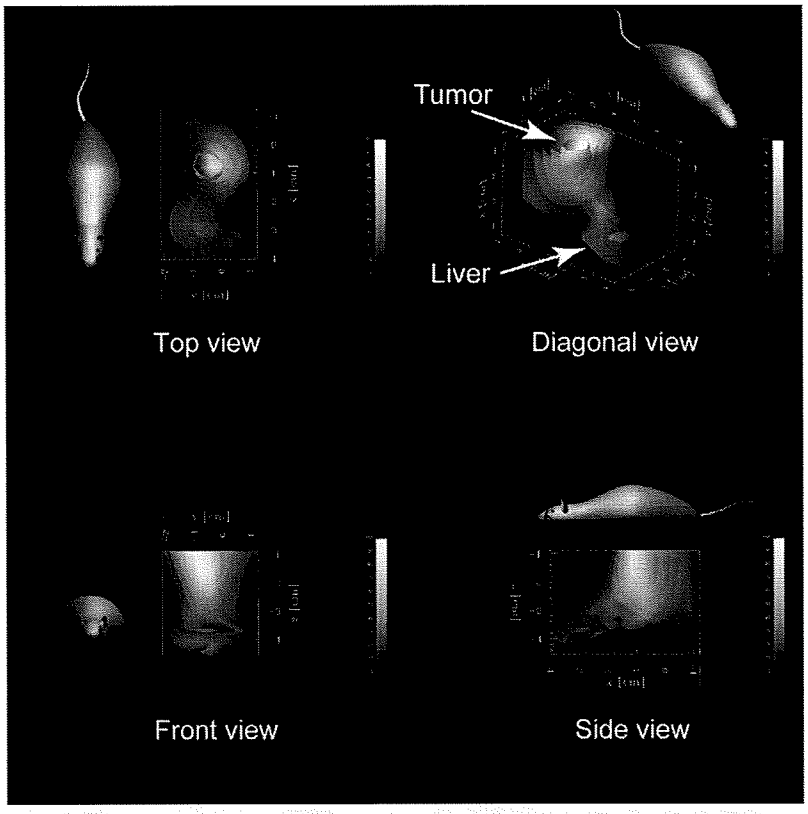

Fig. 7 3D image of ^{65}Zn distributed in the tumor-bearing mouse. The orientations of the sample are indicated by the mouse figures.

active medicines that were simultaneously administered [22]. However, the measurement times taken to obtain the images would be unsuitable for practical imaging, although they can be shortened to about 10 h if more intense γ-ray sources are used. Moreover, a higher spatial resolution would be desired to observe more fine structure. These demands would be met if the γ-ray tracking technique and pulse-shape analysis are implemented, which have been recently developed [23]. With these techniques implemented, the efficiency and the intrinsic characteristics are improved, thereby shortening the measurement time and improving the spatial resolution.

SUMMARY

A prototype of a Compton camera, GREI, has been fabricated for nondestructive imaging of a multi-tracer. It is composed of two double-sided orthogonal-strip Ge detectors, and the efficiency is significant in the energy range from ~200 keV to 2 MeV. The timing method was used to derive the depth position of the γ-ray interaction with a resolution of ~1 mm FWHM. Both analytical and iterative image reconstruction methods were implemented for 2D and 3D imaging. A test experiment was performed to demonstrate the capability of the GREI system. The resulting images successfully visualized the different behavior of each nuclide for both the soybean and the mouse sample. Furthermore, 3D images were obtained even though the samples were measured from a fixed direction. However, there was some distortion in the 3D images, which may have been caused by the use of spatially invariant PSFs. Spatially variant PSFs should be incorporated to obtain more accurate 3D images. To make the GREI

system suitable for practical imaging, γ-ray tracking technique and pulse-shape analysis should be implemented.

ACKNOWLEDGMENTS

This work was supported by a Grant-in-Aid for Scientific Research of the Ministry of Health, Labour and Welfare of Japan and by a Grant for Nano Medicine Research of the New Enegy and Industrial Technology Development Organization of Japan. We thank Dr. R. Hirunuma and Dr. H. Takeichi for supporting the technical treatments.

REFERENCES

1. S. Ambe, S. Y. Chen, Y. Ohkubo, Y. Kobayashi, M. Iwamoto, M. Yanokura, F. Ambe. *Chem. Lett.* **20**, 149 (1991).
2. H. Haba, D. Kaji, Y. Kanayama, K. Igarashi, S. Enomoto. *Radiochim. Acta* **93**, 539 (2005).
3. S. Enomoto. *Biomed. Res. Trace Elem.* **16**, 233 (2005).
4. V. Schönfelder, A. Hirner, K. Schneider. *Nucl. Instrum. Methods* **107**, 385 (1973).
5. R. W. Todd, J. M. Nightingale, D. B. Everett. *Nature* **251**, 132 (1974).
6. G. W. Phillips. *Nucl. Instrum. Methods B* **99**, 674 (1995).
7. Y. F. Yang, Y. Gono, S. Motomura, S. Enomoto, Y. Yano. *IEEE Trans. Nucl. Sci.* **48**, 656 (2001).
8. Y. F. Yang, Y. Gono, S. Motomura, S. Enomoto, Y. Yano. *Nucl. Instrum. Methods A* **482**, 806 (2002).
9. M. Momayezi, W. K. Warburton, R. Kroeger. *Proc. SPIE-Int. Soc. Opt. Eng.* **3768**, 530 (1999).
10. M. Amman, P. N. Luke. *Nucl. Instrum. Methods A* **452**, 155 (2000).
11. E. A. Wulf, J. Ampe, W. N. Johnson, R. A. Kroeger, J. D. Kurfess, B. F. Phlips. *IEEE Trans. Nucl. Sci.* **49**, 1876 (2002).
12. E. A. Wulf, B. F. Phlips, W. N. Johnson, R. A. Kroeger, J. D. Kurfess, E. I. Novikova. *IEEE Trans. Nucl. Sci.* **50**, 1182 (2003).
13. S. Motomura, S. Enomoto, H. Haba, K. Igarashi, Y. Gono, Y. Yano. *IEEE Trans. Nucl. Sci.* **54**, 710 (2007).
14. S. Kabuki, K. Hattori, R. Kohara, E. Kunieda, A. Kubo, H. Kubo, K. Miuchi, T. Nakahara, T. Nagayoshi, H. Nishimura, Y. Okada, R. Orito, H. Sekiya T. Shirahata, A. Takada, K. Ueno. *Nucl. Instrum. Methods A* **580**, 1031 (2007).
15. R. C. Rohe, M. M. Sharfi, K. A. Kecevar, J. D. Valentine, C. Bonnerave. *IEEE Trans. Nucl. Sci.* **44**, 2477 (1997).
16. P. Gilbert. *J. Theor. Biol.* **36**, 105 (1972).
17. W. H. Press, S. A. Teukolsky, W. T. Vetterling, B. P. Flannery. *Numerical Recipes in C: The Art of Scientific Computing*, 2nd ed., p. 681, Cambridge University Press, Cambridge (1992).
18. GEANT, Detector Description and Simulation Tool, CERN, Geneva (1993).
19. H. Tamano, S. Enomoto, B. Liu, A. Takeda. *Biomed. Res. Trace Elem.* **12**, 96 (2001).
20. H. Tamano, S. Enomoto, N. Oku, A. Takeda. *Nucl. Med. Biol.* **29**, 505 (2002).
21. A. Takeda, H. Tamano, S. Enomoto, N. Oku. *Cancer Res.* **61**, 065 (2001).
22. S. Motomura, Y. Kanayama, H. Haba, Y. Watanabe, S. Enomoto. *J. Anal. At. Spectrom.* **23**, 1089 (2008).
23. K. Vetter, M. Burks, L. Mihailescu. *Nucl. Instrum. Methods Phys. Res., Sect. A* **525**, 322 (2004).

Multiple molecular simultaneous imaging in a live mouse using semiconductor Compton camera†

Shinji Motomura,[a] Yousuke Kanayama,[a] Hiromitsu Haba,[b] Yasuyoshi Watanabe[b] and Shuichi Enomoto*[ab]

Received 20th February 2008, Accepted 11th June 2008
First published as an Advance Article on the web 8th July 2008
DOI: 10.1039/b802964d

We have demonstrated the feasibility of semiconductor Compton cameras for multiple molecular imaging in nuclear medicine. The Compton camera used in this work comprises two double-sided orthogonal-strip germanium detectors, and their excellent energy resolution enabled discrimination of the nuclides and accurate determination of the scattering angle for γ rays in wide energy range. Three radioactive tracers of $^{65}ZnCl_2$, $^{85}SrCl_2$, and iodinated (^{131}I) methylnorcholestenol were injected to a living mouse and were measured simultaneously. Both two- and three-dimensional images of each tracer were obtained by a fixed-angle imaging with a single Compton camera, which reflected the different *in vivo* behavior of them.

Introduction

Molecular imaging technology has extended the nuclear medical imaging modalities to visualize specific biological functions and processes in living subjects. The established nuclear medical imaging technologies, namely positron emission tomography (PET) and single photon emission computed tomography (SPECT), have already achieved great success in clinical application because they can conduct noninvasive metabolic imaging in deep tissue. Since PET utilizes coincidence measurement of a pair of 511 keV annihilation photons of a positron and an electron, it provides images of PET imaging agents with high sensitivity, high resolution and high quantitation. On the other hand, SPECT can obtain images of γ-ray emitting tracers with energy less than ~300 keV, though it needs mechanical collimators to determine the lines of projection. Thus, molecular imaging can be realized by labeling the γ-ray- or positron-emitting radionuclides on a specific molecular probe, which is a natural extension of nuclear medicine. The imaging modalities are extensively used for the visualization of changes in the anatomy and function of various organs in several different disorders as well as in following abnormalities or treatment effects longitudinally.

The next extension of the nuclear medicine would be multiple molecular imaging that can provide multidimensional images of correlated molecular events. As most people admit, biological processes in living subjects are quite complex. Thus, a single molecular probe may not be able to characterize the targeted disease or biological function, that is, one may need to use

[a]*Molecular Imaging Research Program, RIKEN Kobe Institute, Chuo-ku, Kobe, Hyogo, 650-0047, Japan. E-mail: motomura@riken.jp*
[b]*Metallomics Research Unit, RIKEN Wako Institute, Wako, Saitama, 351-0198, Japan. E-mail: semo@riken.jp*

† Presented at the International Symposium on Metallomics 2007, Nagoya, Japan, November 28–December 1, 2007.

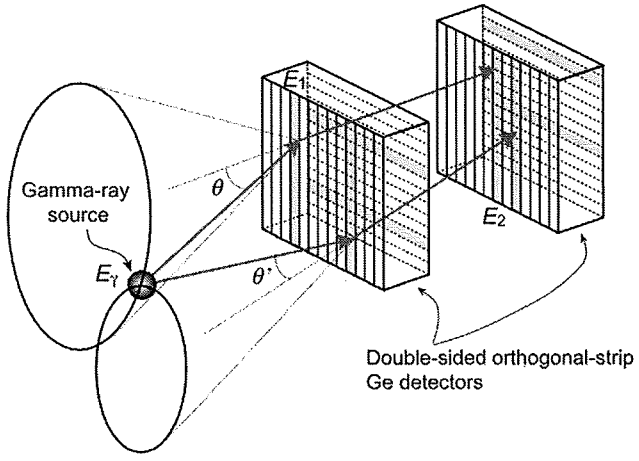

Fig. 1 Schematic diagram of the principle of γ-ray imaging with the GREI apparatus.[2]

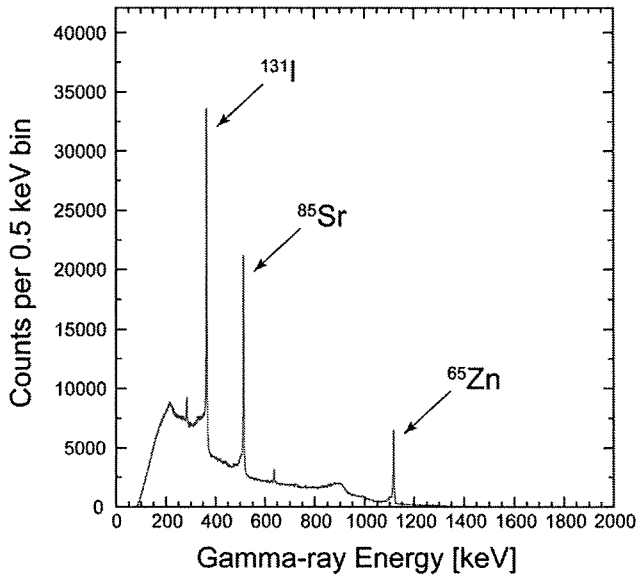

Fig. 2 Measured γ-ray energy spectrum. The tracers of ^{65}Zn, ^{131}I, and ^{85}Sr were clearly identified by the 1115.5, 364.5 and 514.0 keV photopeaks, respectively.

multiple molecular probes at the same time. This also means that more advanced and accurate diagnosis would be possible if we can simultaneously use multiple molecular probes with different characteristics. However, PET would not be suitable for multiple molecular imaging, because it works only for positron emitting nuclides and it is difficult to distinguish them. Though multiple tracer imaging by SPECT has been attempted, the γ-ray energy is limited to less than ~300 keV, which also limits the choice of radionuclides for labeling while there are more choices of radionuclides available.[1]

The GREI apparatus,[2] which is a semiconductor Compton camera named after γ-ray emission imaging, is a promising γ-ray imager being developed for multiple molecular imaging. It is composed of two double-sided orthogonal-strip germanium detectors arranged in parallel (Fig. 1), and the excellent energy resolution allows discrimination of each nuclide simultaneously injected. Furthermore, since Compton cameras need no mechanical collimators, there is no loss of γ rays caused by the collimation, and multidirectional projection of the γ-ray source distribution can be obtained even by fixed-angle imaging with

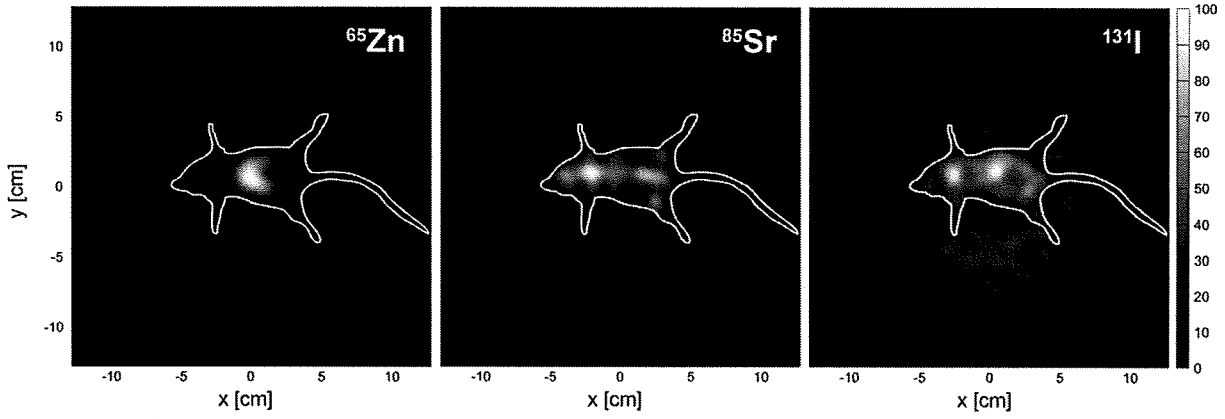

Fig. 3 Results of 2D image reconstruction.

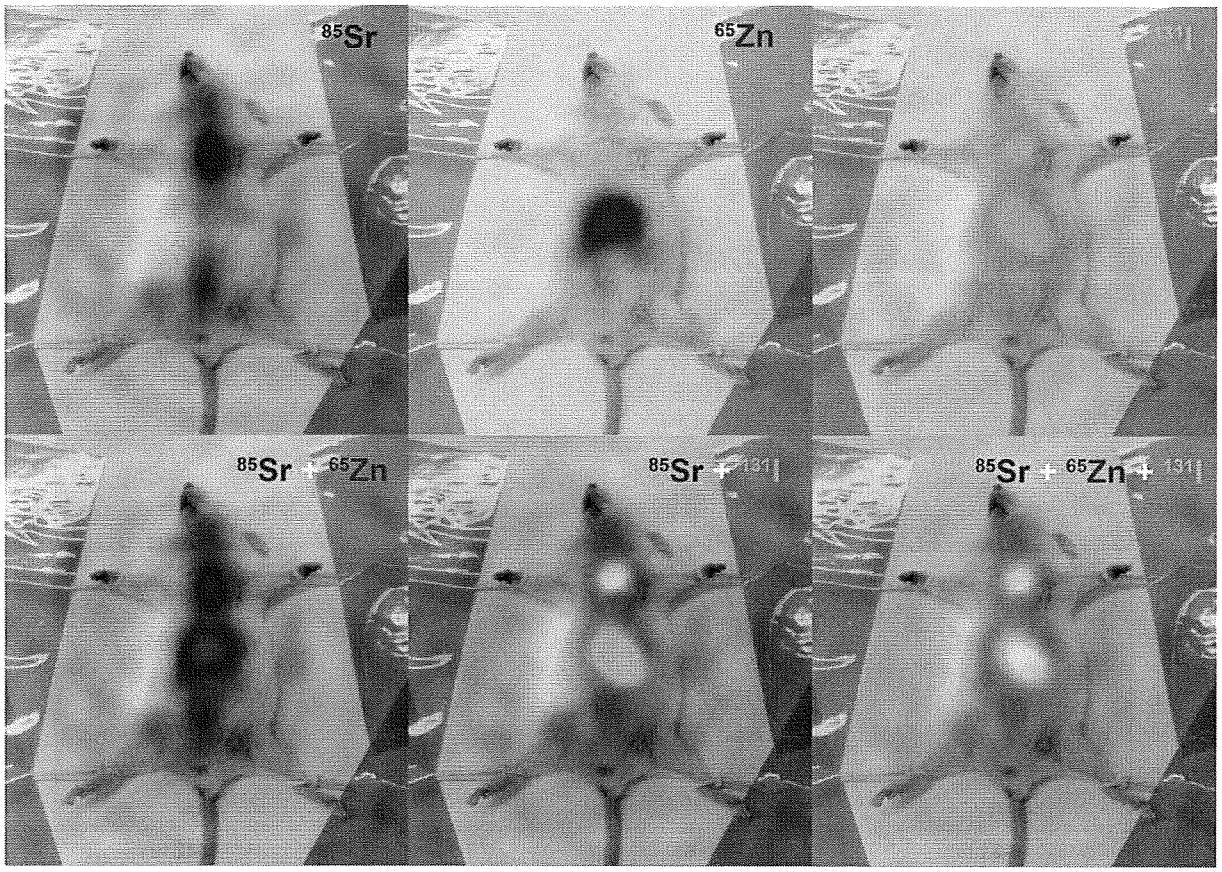

Fig. 4 Example of representing the 2D reconstructed images.

